Applied Surface Science 638 (2023) 158121

Contents lists available at ScienceDirect

Applied Surface Science

journal homepage: www.elsevier.com/locate/apsusc

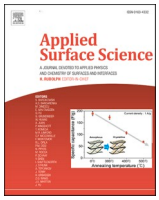

Full Length Article

Kinetic study of hybrid supercapacitor using transition metal quantum dots @ graphenes composite as a model electrode

Yaoning Xi [a,b,c], Jingwang Yan [b,c], Baigang An [a,*]

[a] Key Lab of Energy Materials and Electrochemistry Liaoning, School of Chemical Engineering, University of Science and Technology Liaoning, Qianshanzhong Road 189, Anshan 114051, China
[b] Division of Energy Storage, Dalian Institute of Chemical Physics, Chinese Academy of Sciences, Zhongshan Road 457, Dalian 116023, China
[c] Dalian National Laboratory for Clean Energy, Zhongshan Road 457, Dalian 116023, China

ARTICLE INFO

Keywords:
Transition metal quantum dots
Graphene
Supercapacitor
Quantum chemistry
Electrode reaction kinetics

ABSTRACT

In this study, a series of materials with electric double-layer capacitance (EDLC) and pseudocapacitance (PC) have been prepared by adjusting the functional groups and anchoring transition metal quantum dots (TMQDs) on the surface of reduced graphene oxide (rGO) by chemical bonds. The nano-sized TMQDs interlayered in rGOs can contribute a large portion of PC, meanwhile rGOs supply the EDLC to the hybrid supercapacitor. Electrochemical testing results demonstrated that the Fe/Co/Ni TMQDs anchored the rGO (Fe/Co/Ni-TMQD@rGO) exhibited the improved capacitive and rate performances. To elucidate the reaction kinetics of the electrodes, the capacitance contributions of diffusion-controlled processes (DCPs) and surface-controlled processes (SCPs) were separated by the theoretical calculation. It was found that the capacitance contributed by the DCPs is closely related with the number of the valence electrons of the iron group transition metal elements (ITMEs). The ITMEs with more valence electrons exhibited the higher DCPs contribution to the capacitance of the composite. Further, the quantum chemical calculation results suggested that OH^- adsorption energy is deeply related to the contribution proportion of SCP to the total capacitance. The discovered mechanism supplies a guidance to the design and development of novel composite electrode materials for hybrid supercapacitors.

1. Introduction

Supercapacitors featuring the high power density and excellent rate performance have been attracting more and more attentions. According to energy storage mechanism, the electrode materials for supercapacitors can be divided into three types: electric double layer capacitance (EDLC), pseudocapacitance (PC) and hybrid capacitance (HC) combining EDLC and PC [1]. Among these materials, HC materials are specially promising because they combine the advantages of EDLC with rapid charge and discharge capability and the PC with high specific capacitance [2,3]. Iron group transition metals elements (ITMEs) have similar outer electronic structure ($3d^{6\text{-}8}4\ s^2$) leading them easy to coordinate with C, O or N atoms [4,5]. However, some of the valence electrons of ITMEs are less likely to participate in forming the coordination bonds, because the number of electrons occupying the 3d orbital of ITMEs is more than 5, which would lead ITMEs to compose the composites to exhibit the higher electrochemical activity [6,7].

Carbon materials generally have large specific surface area and tunable pores, and thus are widely used as EDLC materials [8]. Meanwhile some carbon materials with good conductivity are also used as the substrate for HC materials to load the pseudocapacitive materials by multiple intermolecular forces [9–13]. Due to the interaction of π-π bond and van der Waals force, graphenes often suffer from serious agglomeration and stacking, which severely blocks the diffusion of electrolyte ions between graphene layers and makes the electrochemical active sites in graphene difficult to be accessed when graphenes are used as the electrode materials [14]. Some techniques such as intercalation, template-assisting and extrusion of graphene have been used to prevent graphene sheets from agglomeration [15–17]. Ma et al. prepared a two-dimensional Ni-Co hydroxide nanosheets by the hydrothermal method and combined it with rGO to prepare the ultra-thin nanocomposites [18]. The mountain-like Ni/Co-OH/rGO electrodes exhibited a high specific capacitance of 1691F g^{-1} at 0.5 A g^{-1}, with cycling stability (80% retention after 1000 cycles). The Ni/Co-OH nanosheets with the thickness of 1.37 nm were acted as intercalations of rGO to help the nanocomposite to achieve extraordinary EDLC and PC performance.

* Corresponding author.
E-mail address: bgan@ustl.edu.cn (B. An).

https://doi.org/10.1016/j.apsusc.2023.158121
Received 14 June 2023; Received in revised form 20 July 2023; Accepted 26 July 2023
Available online 27 July 2023

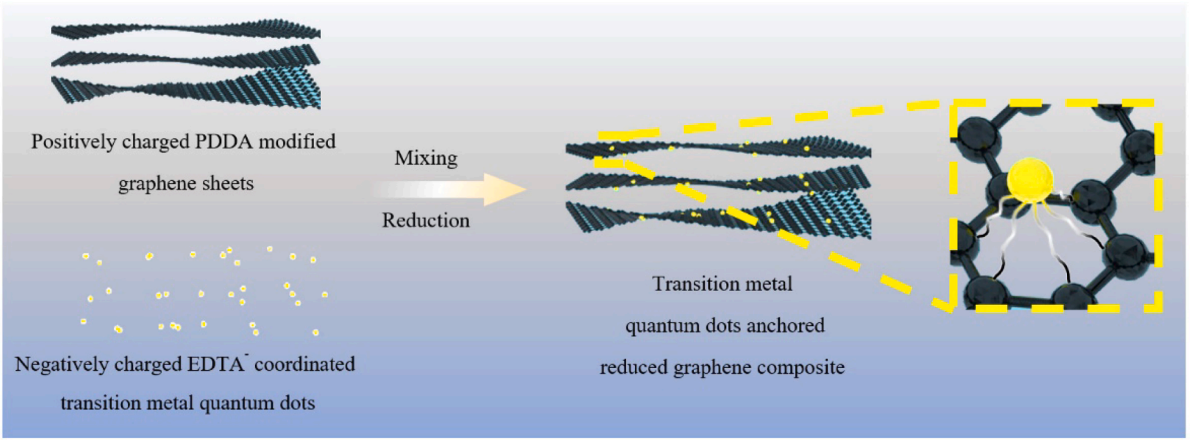

Scheme 1. Schematic diagram of the preparation process of the TMQD@rGO nanostructured composites.

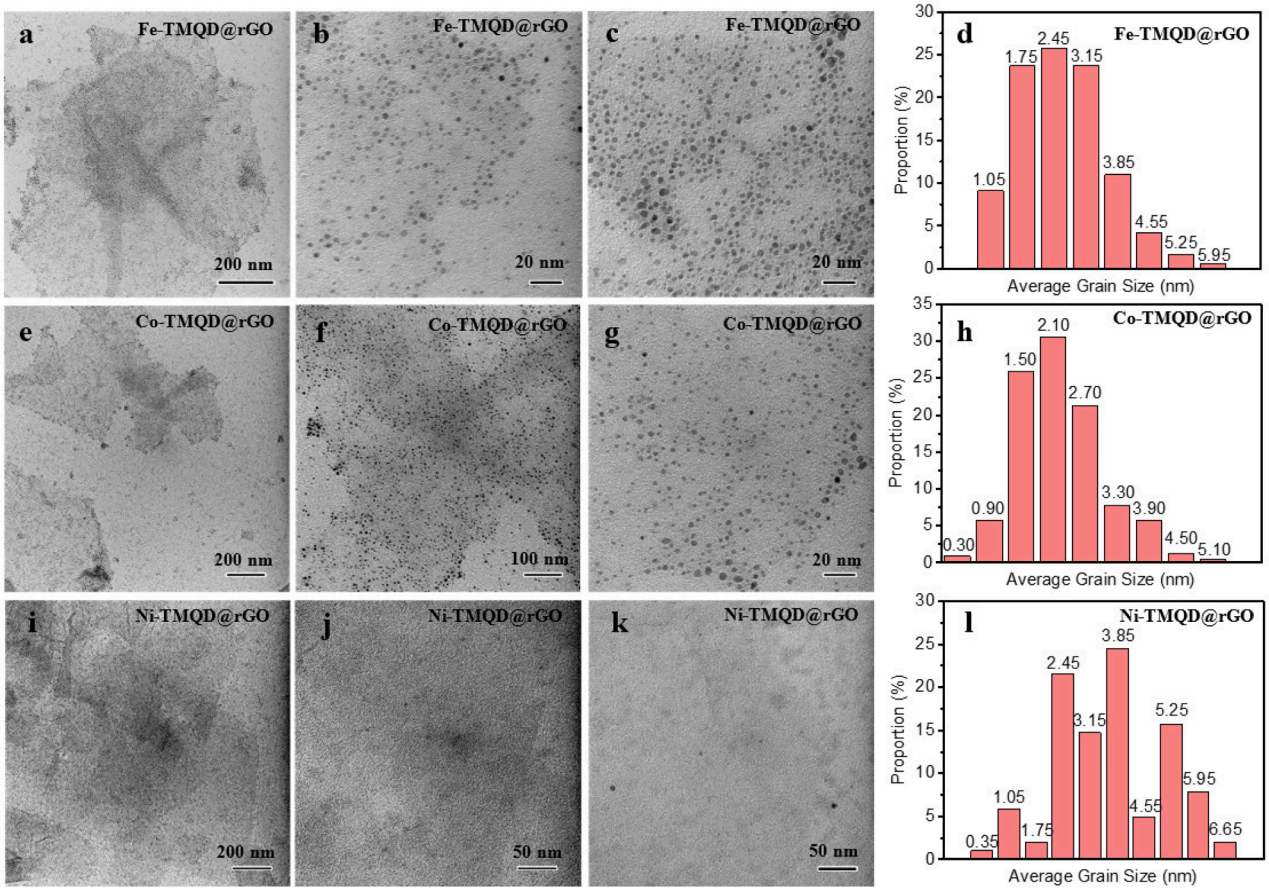

Fig. 1. TEM image of the transition metal quantum dots uniformly anchored to the surface of rGO and the statistical distribution of quantum dots size. (a)-(d) Fe-TMQD@rGO; (e)-(h) Co-TMQD@rGO; (i)-(l) Ni-TMQD@rGO.

However, the electrode reaction kinetics about the diffusion-controlled processes (DCPs) and surface-controlled processes (SCPs) were not investigated and discussed. Zhang et al. prepared a nanocomposite of $NiCo_2O_4$@rGO by chemical reduction of graphene oxide (GO) onto the surface of $NiCo_2O_4$ substrates to enhance the conductivity of the nanocomposite [19]. The specific capacitance of the $NiCo_2O_4$@rGO reached 3.6 F/cm^2, and the capacity retention rate was 90% after 1000 cycles. Wang et al. prepared the nanocomposites of Fe_3O_4 with one-dimensional carbon nanotubes or two-dimensional rGO nanosheets by hydrothermal method. The specific capacitance of the Fe_3O_4/rGO reached 220.1 F/g and the capacity retention rate was 90% after 3000 cycles, which was much better than the Fe_3O_4/CNTs (119.5 F/g) [20]. The results suggested that graphenes were an appropriate substrate material to improve the capacitive behaviors of metal compounds. However, the interactions between graphenes and metal compounds have not been investigated when they are used as EDLC and PC materials, respectively. Therefore, it is necessary to develop the model materials to deeply study the electrode reaction mechanisms by modern characterization methods. Here, a series of nanocomposites that the iron group transition metal quantum dots of Fe, Co and Ni intercalated rGO were prepared and used as model

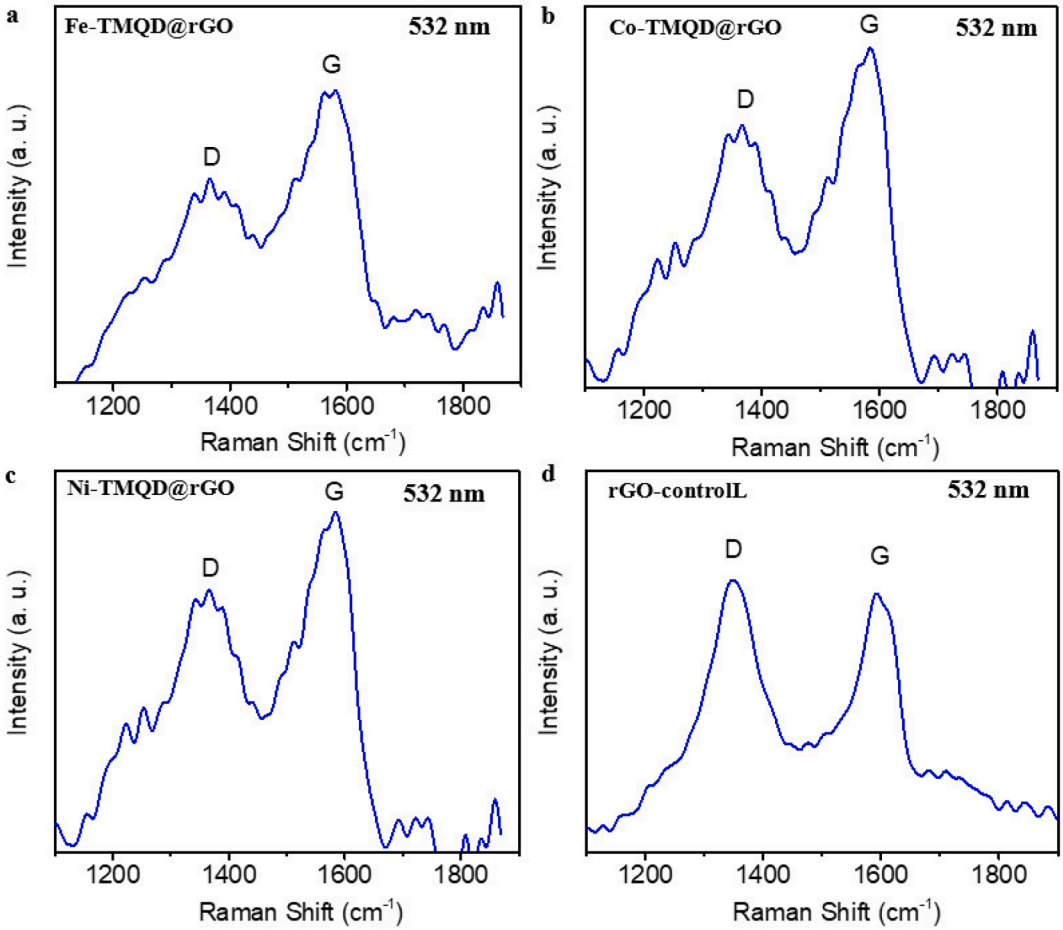

Fig. 2. Raman spectra of the (a) Fe-TMQD@rGO; (b) Co-TMQD@rGO; (c) Ni-TMQD@rGO; (d) rGO-control sample.

electrodes.

The theory study of supercapacitor electrode reaction kinetics with classical electrochemical methods is mainly focused on the relationship between electrode reaction rate, electrode potential and electrolyte concentration. Although researchers have studied the redox reaction processes and the effect of diffusion processes on the electrode reaction of HC materials [21–23], the reaction kinetics study of DCPs and SCPs for HC materials is still insufficient [24–28]. Notably, the reaction kinetics of HC materials mainly involves DCPs and the SCPs in essence [29,30], highlighting the importance of further researches in this area. In this study of the Fe/Co/Ni-TMQD@rGO composites, the contribution of DCPs and SCPs to capacitance were fitted and calculated to find out the interaction between the two processes, and the relationship between the number of valence electrons of ITMEs and the contribution ratio of pseudocapacitance in the model materials.

To elucidate the reaction kinetics, homemade python program was applied to deal with the mathematical problems. The relationship between the SCP contribution and the number of valence electrons of ITMEs, and the correlation of the adsorption energy of OH^- with the iron group transition metal composites and the SCP contribution were studied for the first time. Electrochemical tests and quantum chemistry calculations results proved that the constructed HC model electrode was helpful to understand and develop the supercapacitors with high performance.

2. Materials and methods

2.1. Materials preparation

The polymer containing specific functional groups was introduced onto graphene surface, then a certain amount of transition metal precursor solution was mixed with the graphene solution, followed by adding the reducing agent into the mixed solution. During the reduction process, the TMQDs were anchored onto the surface of the rGO sheets by chemical bonds. After washing and drying, the final product of Fe/Co/Ni-TMQD@rGO composites were obtained.

In a typical procedure, rGO mixed solution was prepared by the following steps. Firstly, 10 mg of graphene oxide (GO, Shandong Ou Bo New Materials Co., LTD) were dissolved in 20 ml ultrapure water and stirred for 24 h. At the same time, 0.29 ml of 35 wt% Poly dimethyl diallyl ammonium chloride (PDDA), 50 mg of aminomethane (Tris) and 24 mg of NaCl were dissolved in 20 ml of ultrapure water, and kept stirring for 24 h. Then, all the above solutions were mixed with 32 mg of ascorbic acid and stirred in a water bath at 90 °C for 10 h. The mixed solution was named as solution A. Then Fe/Co/Ni-TMQD@rGO were prepared by the following steps. Firstly, 0.1 mmol of transition metal nitrate hydrate ($Fe(NO_3)_3{\cdot}9H_2O$, $Co(NO_3)_2{\cdot}6H_2O$ or $Ni(NO_3)_2{\cdot}6H_2O$) was dissolved in 10 ml ultrapure water. At the same time, 0.1 mmol of ethylene diamine tetraacetic acid (EDTA-H),160 μl of 35 wt% $NH_3{\cdot}H_2O$ were dissolved in 10 ml of ultrapure water. Then the as-prepared solutions were mixed and stirred at 25 °C for 1 h, and the mixed solution was named as solution B. Solution A and B were cooled down to 0 °C and mixed with each other by vigorous stirring for 1 h and was named as solution C. Then 20 ml of 0.5 M $NaBH_4$ solution was mixed with solution

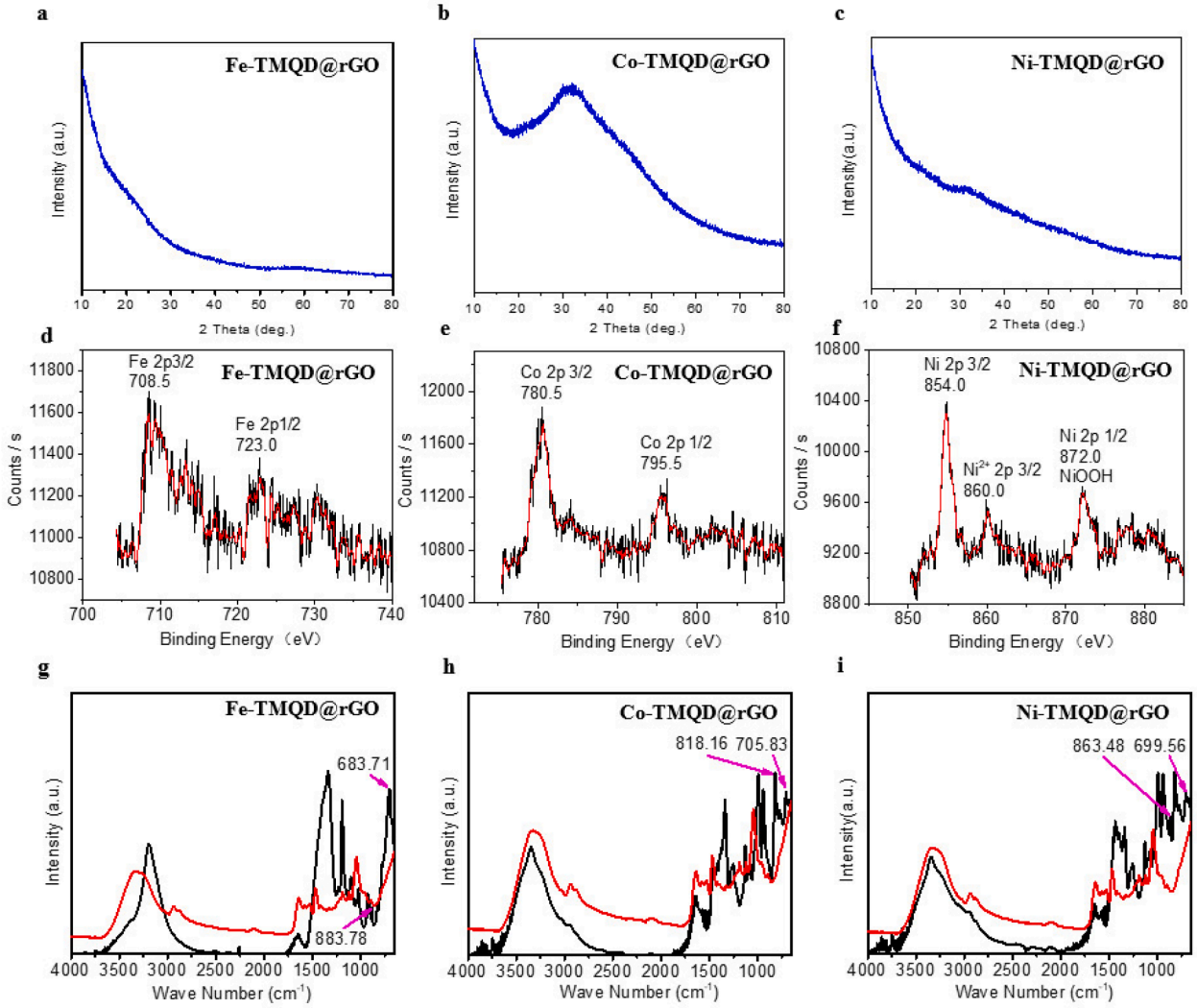

Fig. 3. XRD, XPS, FT-IR spectra. (a)-(c) XRD patterns of Fe/Co/Ni-TMQD@rGO; (d)-(f) XPS spectra of Fe/Co/Ni-TMQD@rGO; (g)-(i) FT-IR spectra of Fe/Co/Ni-TMQD@rGO (red curves are the rGO-control sample).

C, and kept stirring at 0 °C for 2 h. After the reduction reaction, the final solution was obtained and named as solution D, and Fe/Co/Ni-TMQD@rGO composites were collected after being washed by ultrapure water and dried at 80 °C in air atmosphere. The contrast electrodes were prepared by the same method except that there was no transition metal nitrate hydrate added in solution B and was named as rGO-control sample.

2.2. Characterization of microstructures and physical properties

The transition electronic microscopy (TEM) measurements were performed on a JEOL JEM 1200 TEM microscope with an acceleration voltage of 100 kV. The samples were dispersed in anhydrous ethanol and dropped onto a copper grid, then dried at room temperature. Raman spectroscopy measurements were performed with a JPK Nano Wizard Ultra Speed & Renishaw in Via Raman microscope system with a Leica 50x objective lens and a laser excitation wavelength of 532 nm. The incident laser powers were carefully tuned to avoid sample damage or laser induced heating and the measurements were conducted with around 0.33 mW incident laser power. Raman spectra were collected with an acquisition time of 120 s. X-ray diffraction (XRD) patterns were obtained on a Bruker D8 Advance X-ray diffractometer with CuKα radiation over the 2θ from 10° to 80° at the scanning rate of 10° min^{-1}. The FT-IR experiment was carried out on a Nicolet-6700 type FT-IR spectrometer (Thermo Fisher Scientific Ltd.) in a KBr pellet, scanning from 4000 to 400 cm^{-1} at room temperature. Chemical state of sample surface was analyzed by X-ray photoelectron spectroscopy (XPS, Thermo Multi-Lab 2000 spectrometer).

2.3. Electrochemical measurements

Electrochemical measurements of samples were performed by using a VMP-300 electrochemical test station (Bio-logic Science Instruments) at room temperature. A three-electrode electrochemical cell containing 3.0 M KOH aqueous solution was used. The Pt foil with surface area of 4 cm^2 and the saturated calomel electrode (0.2412 V VS SHE) were used as the counter and reference electrode, respectively. The working electrodes were prepared by the following method. Firstly, 20 ml of solution D was washed, dried and re-dispersed in 20 ml of ultrapure water. Then, 1.5 ml of the re-dispersed solution was mixed with 0.5 ml of anhydrous ethanol and 50 μl of 5 wt% nafion solution with vigorous stirring for 2 h. Finally, 50 μl of suspension was dropped onto the surface of a glassy carbon electrode with diameter of 4.0 mm. The loading amount of the Fe/Co/Ni-TMQD@rGO and the rGO-control were 2.16 mg, 1.82 mg, 1.56 mg, and 4.96 mg, respectively. Electrochemical impedance (EIS) tests of samples were performed in a frequency range between 500 kHz and 100 mHz at an amplitude of 5 mV in a fully charged condition. EIS data were analyzed using Zview software (Scribner Associates, USA).

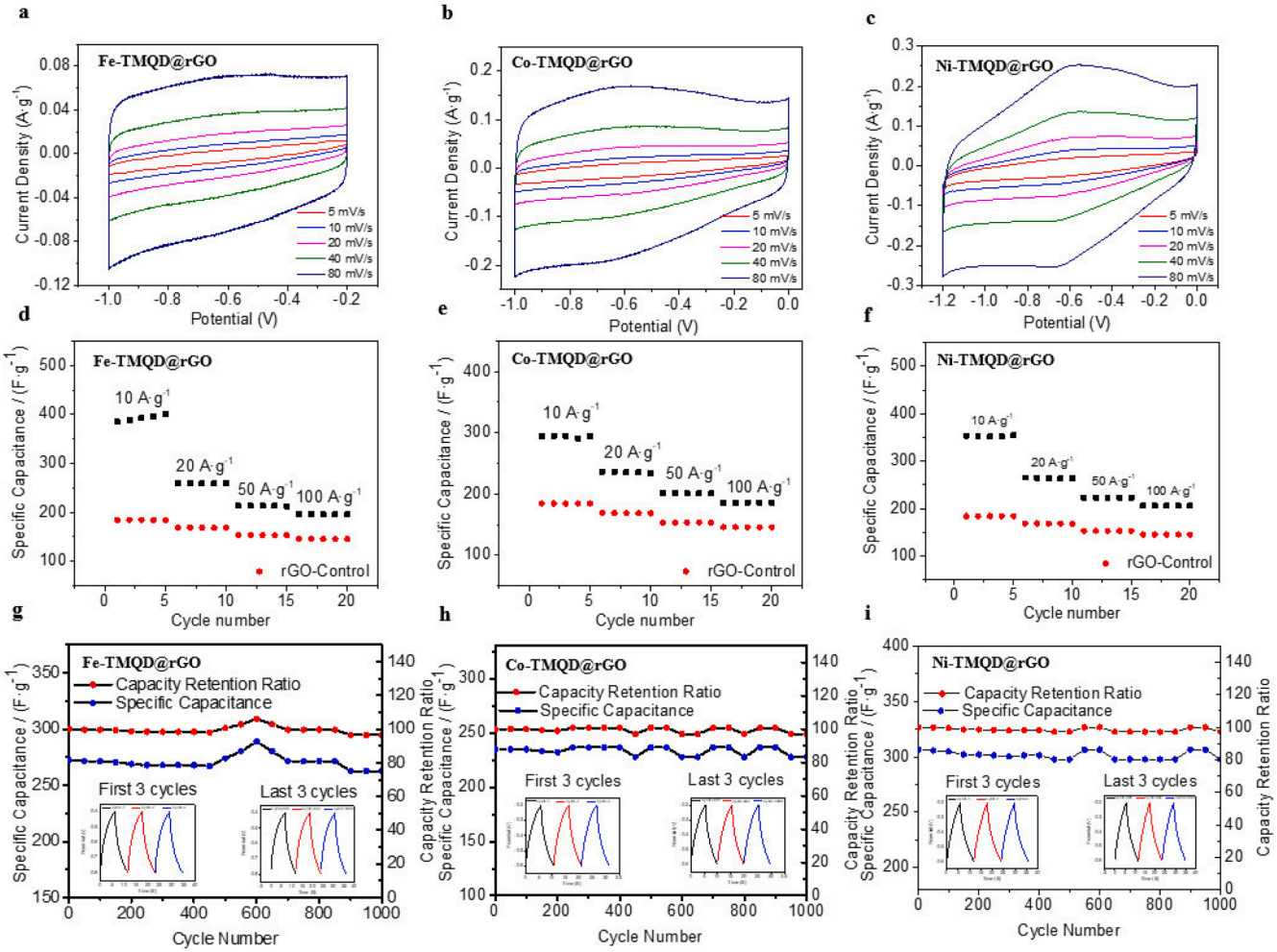

Fig. 4. (a)-(c) CV curves of Fe/Co/Ni-TMQD@rGO electrodes, (d)-(f) Rate performance of Fe/Co/Ni-TMQD@rGO electrodes and the rGO-control electrodes, (g)-(i) GCD curves and the cyclic stability of Fe/Co/Ni-TMQD@rGO electrodes.

Considering the potentials of the water electrolysis and the redox reactions of transition metals of the Fe/Co/Ni TMQDs, the cyclic voltammetry (CV) tests potential ranges for Fe/Co/Ni-TMQD@rGO electrodes were separately carried out in the potential range between −0.2 V to −1.0 V and 0.0 V to −1.0 V and 0.0 V to −1.2 V. Galvanostatic charge–discharge (GCD) tests were separately carried out in the potential range between −0.4 V to −0.8 V, −0.2 V to −0.6 V and −0.2 V to −0.6 V with the charge–discharge current density of 10 A g^{-1}, 20 A g^{-1}, 50 A g^{-1} and 100 A g^{-1}, respectively. Cycling stability tests were carried out in the potential range of −0.4 V to −0.8 V, −0.2 V to −0.6 V and −0.2 V to −0.6 V with a charge–discharge current density of 20 A g^{-1}. The evaluation on the contribution ratio of DCPs and the SCPs to supercapacitor was carried out by a homemade python program. The details for the python program are listed in the supporting information.

All the density functional theory (DFT) calculations were performed with the Perdew–Burke–Ernzerhof (PBE) generalized gradient approximation and the projected augmented wave (PAW) method [31–34] using Vienna Ab initio Software Package (VASP 5.4.1). The cutoff energy for the plane-wave basis set was set to 450 eV. The ultrasoft pseudopotential was employed to describe the interaction between valence electrons and the ionic core. Monkhorst-Pack special k-point meshes of $2 \times 2 \times 1$ were proposed to carry out geometry optimization and electronic structure calculation. During the geometry optimization, all atoms were allowed to relax without any constraints until the convergence thresholds of maximum force and energy were smaller than 0.01 eV/Å and 1.0×10^{-5} eV/atom, respectively. A vacuum layer of 15 Å in thickness was introduced to avoid interactions between periodic images.

3. Results and discussion

3.1. Microstructures and physical properties of the materials

As illustrated in Scheme 1, the wet chemical method was applied to prepare the Fe/Co/Ni-TMQD@rGO composites. The modified rGO and TMQD coordination compounds were selected as basal EDLC material and PC material, respectively. Oxidized graphene surfaces are rich in oxygen-containing functional groups, such as hydroxyl, carboxyl, epoxy, and ester groups, which are negatively charged in aqueous solutions. Poly dimethyl diallyl ammonium chloride (PDDA) molecules, which are strong cationic polyelectrolytes commonly used as anion-capturing agents, can be absorbed onto the surface of oxidized graphene and dissociate chloride ions, resulting in a positively charged modified graphene. On the other hand, ethylene diamine tetraacetic acid (EDTA-H) is a widely used chelating agent that forms coordination complexes with transition metal cations. Due to the presence of uncoordinated oxygen atoms within the coordination complex, the complex exhibits negatively charged. Hence, rGOs modified with PDDA showed positive charges, while TMQDs modified with EDTA-H showed negative charges, resulting in the uniform anchoring of TMQDs onto the surface of rGO by electrostatic attraction. As shown in Fig. 1, TMQDs were homogeneously dispersed on the surface of rGO sheets, and the average size of the Fe, Co, and Ni quantum dots was about 2.6 nm, 2.26 nm, and 6.61 nm,

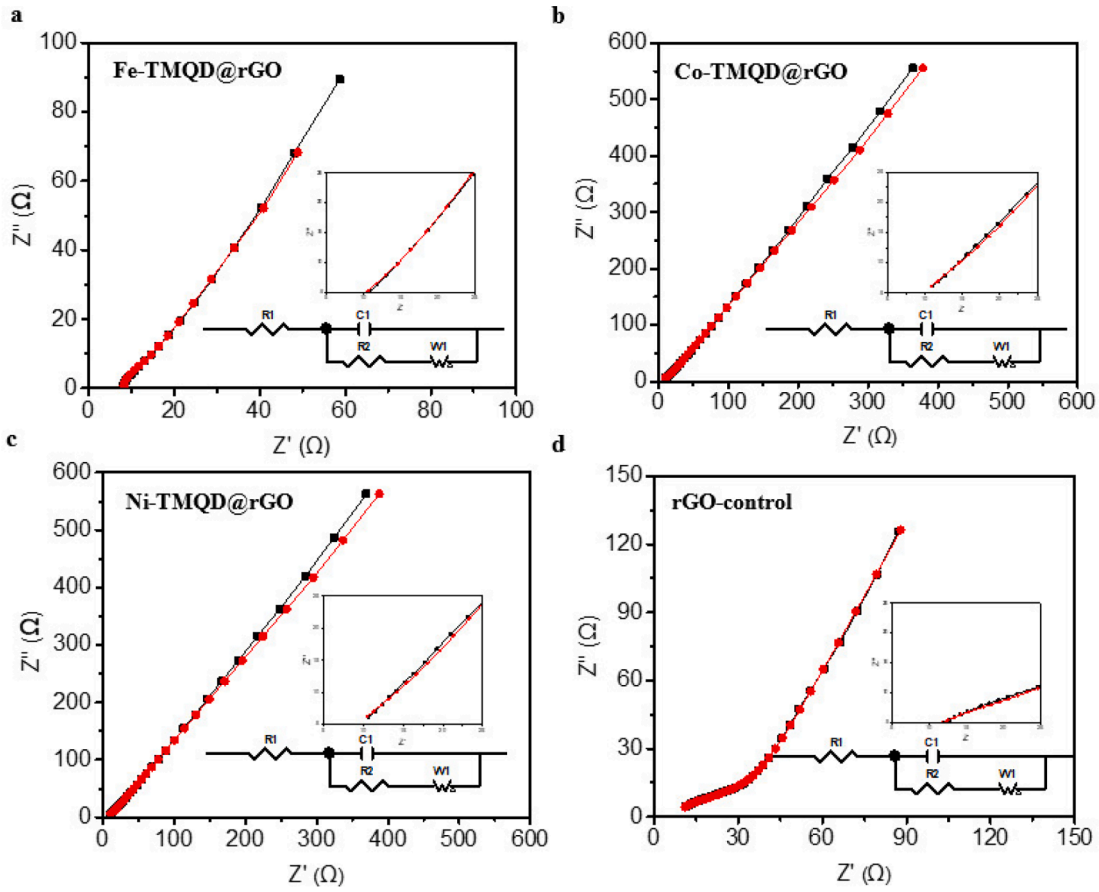

Fig. 5. EIS and the corresponding equivalent circuits of the Fe/Co/Ni-TMQD@rGO electrodes, R1 represents the electric series resistance and R2 represents the resistance of graphene substrate (all red curves are the fit results of the corresponding samples). (a) Fe-TMQD@rGO; (b) Co-TMQD@rGO; (c) Ni-TMQD@rGO; (d) rGO-control electrode.

respectively.

Raman spectroscopy (Fig. 2a and b) can be used to identify the chemical and physical properties of graphene. Peak G is the main characteristic peak of graphene caused by the in-plane vibration of SP^2 electron inside carbon atom, meanwhile peak D is generally considered as the vibration peak of disordered carbon atoms inside graphene. The intensity ratio of peak D to peak G (I_D/I_G) is generally used to quantitatively reflect the defect density in graphene [35]. The Raman spectra showed that the I_D/I_G value of the Fe/Co/Ni-TMQD@rGO samples were 0.6980, 0.7723, and 0.7704 respectively, which were lower than that of rGO-control sample (1.0525). Absorption of the TMQDs on the active sites (defect sites) decreased the defect concentration in graphene, leading to the decrease of I_D/I_G value.

The smooth XRD pattern (Fig. 3a-c) indicated that all as-prepared composites were in an amorphous state, since TMQDs anchored on the surface of the rGO sheets were too small in size to be identified by XRD. As illustrated in the XPS spectra (Fig. 3d-f), the binding energy peaks at 710.5 eV and 724.3 eV of Fe-TMQD@rGO corresponded to Fe $2p^{3/2}$ and Fe $2p^{1/2}$ respectively, indicating that Fe^{3+} existed in the composite. Furthermore, FT-IR spectra showed the peaks at 883.78 cm^{-1} corresponded to the Fe-O chemical bond, and the peak at 683.71 cm^{-1}corresponded to the Fe-N chemical bond, which proved that iron ions were bonded with oxygen and nitrogen in the composite. Similarly, the binding energy peaks displayed at 780.5 eV and 795.9 eV in the spectra of Co-TMQD@rGO corresponded to the Co $2p^{3/2}$ and Co $2p^{1/2}$ respectively, suggesting the presence of $Co^{3+}$and Co^{2+} in the composite. Additionally, the the peaks at 705.83 cm^{-1} and 818.16 cm^{-1} in the FT-IR spectrum corresponding to the Co-O and Co-N chemical bonds, inferred that the cobalt ions were bonded with oxygen and nitrogen in the composite. In the same way, the binding energy peaks exhibited at 855.1 eV and 873.1 eV of Ni-TMQD@rGO corresponded to Ni $2p^{3/2}$ and Ni $2p^{1/2}$ respectively, proving the $Ni^{3+}$and Ni^{2+} in the composite. Moreover, the FT-IR spectrum for Ni-TMQD@rGO exhibited the peaks at 699.56 cm^{-1} and 863.48 cm^{-1}, suggesting the Ni-O and Ni-N chemical bonds.

Based on the results obtained from spectroscopic characterization, it can be concluded that the negatively charged $EDTA^-$ coordinated TMQDs were electrostatically anchored onto the surface of positively charged PDDA modified graphene sheets. Thus, the TMQD@rGO composites are consistent with our design for the model electrode, and can be utilized for studying electrochemical reaction kinetics.

3.2. *Electrochemical performance*

The CV curves for Fe/Co/Ni-TMQD@rGO electrodes shown in Fig. 4a-c resemble a rectangular shape, with the redox peaks becoming more pronounced as the scanning speed is decreased. These CV curves suggest that the excellent conductivity of the graphene substrate benefits the fast surface controlled redox reactions, leading to higher pseudocapacitance of TMQDs. The specific capacitances and rate performance of the Fe/Co/Ni-TMQD@rGO and rGO-control electrodes are shown in Fig. 4d-f and listed in Table S1. At the same current density, the specific capacitances of the Fe/Co/Ni-TMQD@rGO electrodes is significantly higher than that of the rGO-control electrodes. Nevertheless, the rGO-control electrode exhibited superior rate performance since the charge–discharge processes on the rGO-control electrode are the absorption and desorption of the electrolyte ions on the surfaces of rGO sheets, which are much faster than the redox reactions of TMQDs.

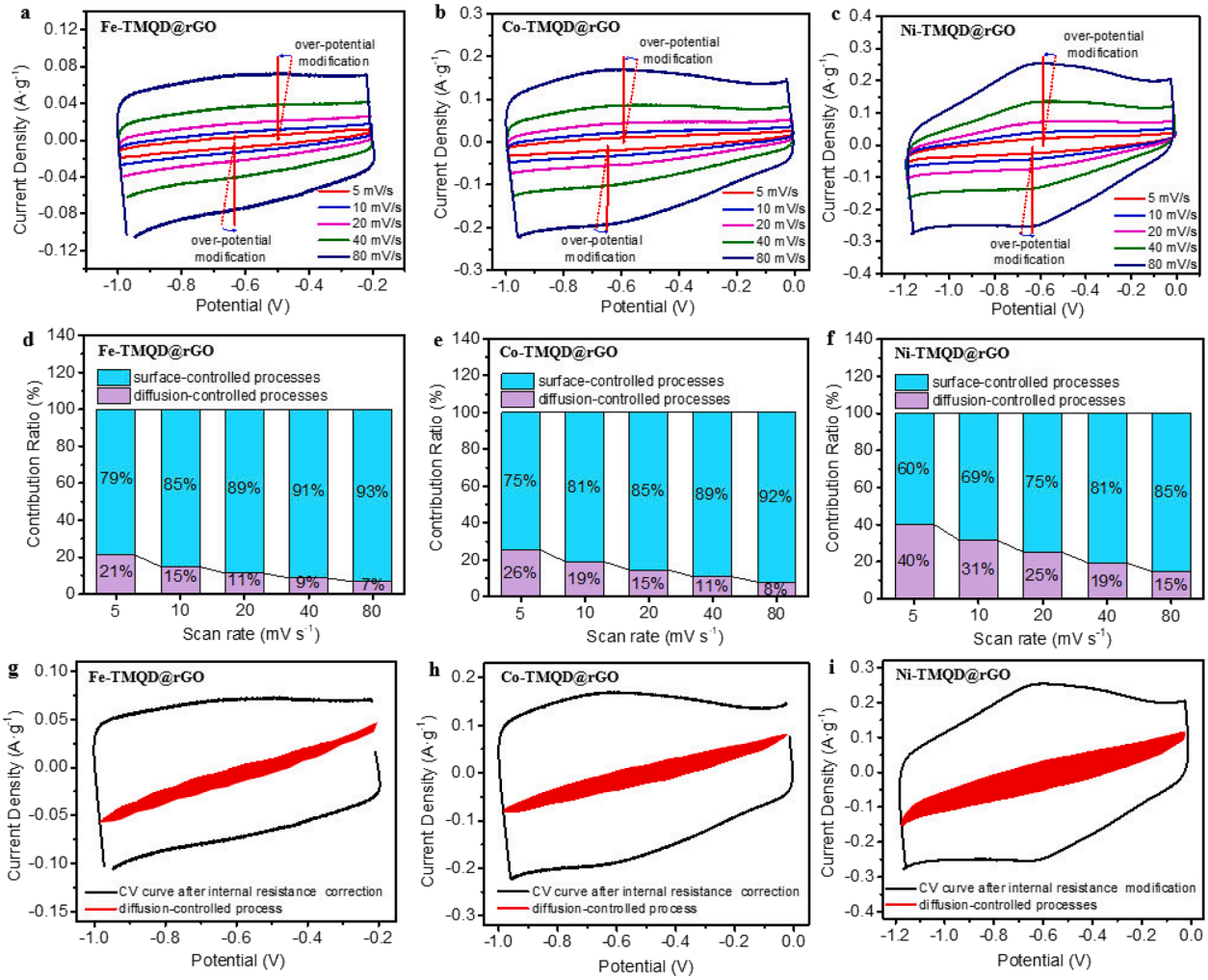

Fig. 6. (a)-(c) modified CV curves of the Fe/Co/Ni-TMQD@rGO electrodes; (d)-(f) SCP and DCP contributions at different scan rates; (g)-(i) CV curves displaying the DCP contribution (red areas) at the scan speed of 80 mV s^{-1}.

Table 1
Calculation results for OH^- adsorption energy.

	Fe-TMQD@rGO	Co-TMQD@rGO	Ni-TMQD@rGO	rGO-control
OH^- ads energy (J)	−5.0571	−4.4837	−3.9126	−0.6312

The galvanostatic charge discharge (GCD) curves and the cyclic stability tests showed that there was no obvious loss of specific capacitance at a current density of 20 A g^{-1} after 1000 cycles (Fig. 4g-i). The impressive cyclic stability of the composite electrodes can be attributed to the 3D structure of TMQD@rGO composites, which enables the electrolyte to fully infiltrate between the graphene layers and provide excellent conditions for the electrochemical oxidation–reduction reactions of TMQDs.

In order to get the internal resistance of the Fe/Co/Ni-TMQD@rGO and rGO-control electrodes, EIS tests were carried out and the results are shown in Fig. 5. The fitting results according to the equivalent circuits are summarized in Table S2. In the equivalent circuits, R1 denotes the electric series resistance of the electrodes, which is associated with the wire resistance, electrolyte conductivity, and microstructure of the electrode materials. The model electrodes prepared in this work possess a 3D spatial structure where the electrolyte can penetrate between the graphene layers, so the Fe/Co/Ni-TMQD@rGO electrodes exhibited the smaller R1 values than the rGO-control electrode. Meanwhile, R2 signifies the electrochemical reaction resistance of the as-prepared electrodes. The results showed that the R2 of the Fe/Co/Ni-TMQD@rGO electrodes is higher than that of the rGO-control electrode. This is because the electrochemical oxidation–reduction reaction rates of the TMQDs anchored on the graphene sheets are substantially slower compared to the fast charge–discharge reaction rates of the graphene substrate.

To further elucidate the relationship between the number of the valence electrons of the ITMEs and the DCPs/SCPs contributions to the capacitance of the model composites, electrochemical kinetics study based on the CV curves was carried out. The contributions of DCPs and SCPs to the total capacitance were calculated by the following equation (eqn. (1)),

$$i(V) = k_1 v + k_2 v^{\frac{1}{2}} \quad (1)$$

where i is the current, v is the scan rate, and k_1 and k_2 are the contributing parameters, $k_1 v$ is the fraction of current determined by the SCPs and $k_2 v^{1/2}$ is that determined by the DCPs. Before distinguishing DCPs and the SCPs of the CV curves, the over-potential on the CV curves should be removed with the flowing equation (eqn. (2)), which was proposed by Cao et. al [36],

$$U_{calibrated} = U_{original} + RI_{original} \quad (2)$$

where $U_{calibrated}$ represents the calibrated voltage, $U_{original}$ represents the original (experimental) voltage, $I_{original}$ represents the original

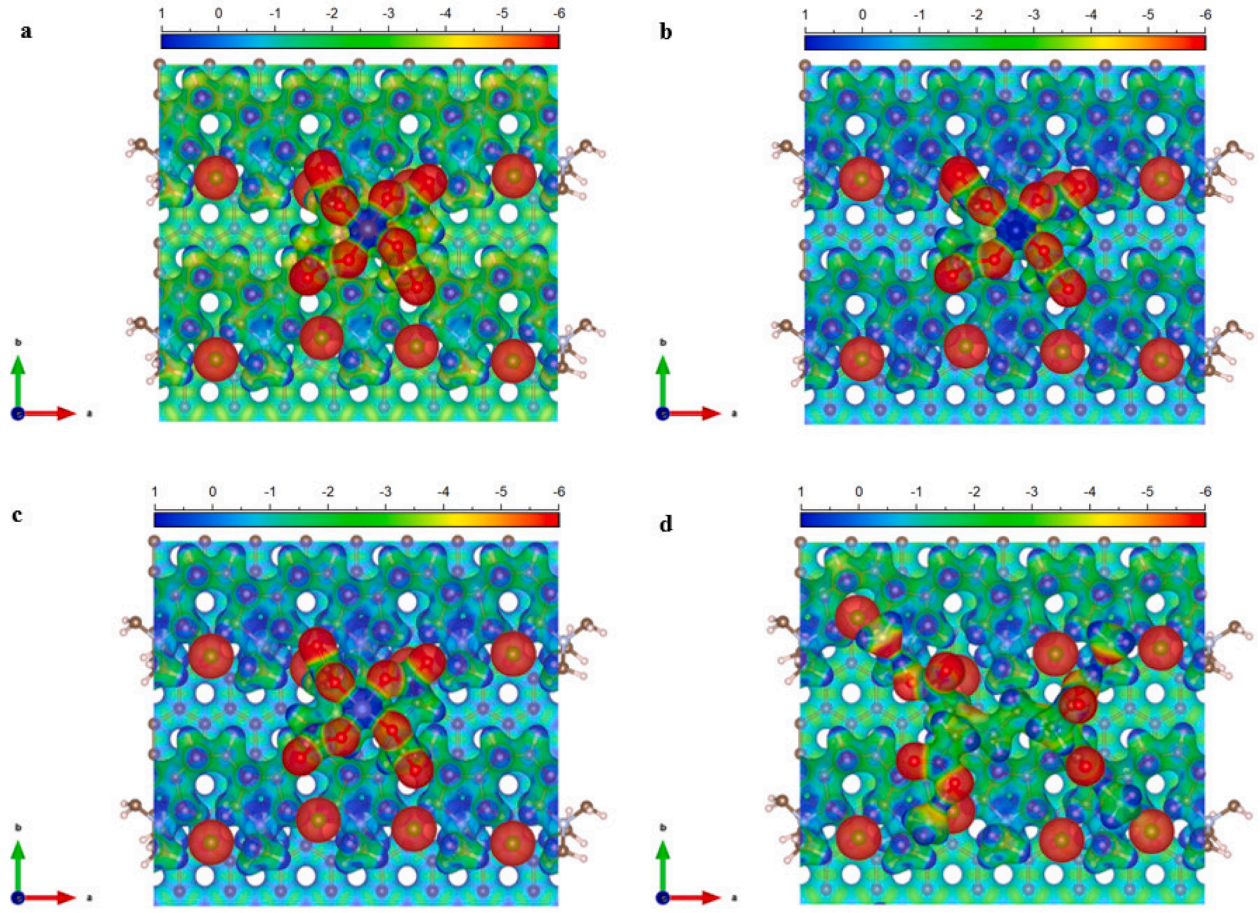

Fig. 7. Simulation results of the electrostatic potential of the Fe/Co/Ni-TMQD@rGO composite materials. (a) Fe-TMQD@rGO; (b) Co-TMQD@rGO; (c) Ni-TMQD@rGO; (d) rGO-control sample. (The red zones have low electrostatic potential and are easily attacked by electrophilic reagents, the blue zones have high electrostatic potential and are easily attacked by nucleophilic reagents).

(experimental) current. The modified CV curves are shown in Fig. 6a-c (corresponding to the Fig. 4a-c). According to the modified CV curves and eqn (1), with the assistance of the homemade python program, the proportions of the SCPs at different scan rates were calculated and summarized in Fig. 6d-f. It can be seen that the SCP contribution always played a dominant role (greater than 60%) in the charge storage process, and with increasing the scan rate the SCP contribution becomes more significant. Taking the scan rate of 80 mV s^{-1} as an example (Fig. 6g-i), the SCPs contributed 93% (Fe-TMQD@rGO electrode), 92% (Co-TMQD@rGO electrode), 85% (Ni-TMQD@rGO electrode) of the total specific capacitance, respectively. As the scan rate increased, the increasing trend of the SCP contribution gradually slowed down, suggesting that at high scanning rates, the diffusion process of the electrochemical reaction in the active materials could reach its limit, and SCPs and DCPs would approach a dynamic equilibrium state.

At the same scanning rates, the contributions to the total capacitance of the DCPs were ascending in the following order: Fe-TMQD@rGO, Co-TMQD@rGO and Ni-TMQD@rGO. It is seen that the greater the number of valence electrons, the higher the contribution proportion of DCPs to the total capacitance. When the Fe/Co/Ni-TMQD@rGO electrodes were tested under different scanning rate, it was found that the contribution of DCPs decreased with increasing the scanning rates, indicating the diffusion rates in the electrodes were not fast enough to meet electrochemical reaction rates. In contrast, the contribution of the SCPs successively increased with raising the scanning rates, indicating that the SCPs were less affected by the fast changing of the electrode potential.

3.3. Influences of OH^- adsorption energy and electrostatic potential on the electrochemical reaction processes

In order to elucidate the electrochemical reaction mechanism associated with the number of valence electrons, OH^- adsorption energy and electronic potential distribution were evaluated for Fe/Co/Ni-TMQD@rGO electrodes by density functional theory (DFT). Fig. S1 showed the molecular structure of the Fe/Co/Ni-TMQD@rGO composites. The simulation results were summarized in Table 1. The calculation results showed that Fe-TMQD@rGO has the highest OH^- adsorption energy, followed by Co-TMQD@rGO and Ni-TMQD@rGO, and rGO has the lowest adsorption energy, indicating that DCPs and SCPs were affected by the adsorption energy of OH^- on the Fe/Co/Ni-TMQD@rGO composites. In other words, the more OH^- ions adsorbed by the ITMEs, the higher the proportion of SCPs contributed to the total capacitance. Fig. 7 showed the simulation results of the electrostatic potential of the Fe/Co/Ni-TMQD@rGO composites. The low electrostatic potential areas in red are easily attacked by electrophilic reagents. The blue regions possess high electrostatic potential and are vulnerable to nucleophiles. The calculations results showed that, compared with the rGO-control structure, Fe/Co/Ni atoms were more likely to adsorb OH^- ions, which facilitated the surface-controlled processes on the surfaces of the Fe/Co/Ni-TMQD@rGO composites.

4. Conclusions

Fe/Co/Ni-TMQD@rGO composites have been successfully prepared by wet chemical method to construct a supercapacitor model electrode.

Electrochemical characterizations and quantum chemistry calculations were carried out to analyze the electrode reaction kinetic in the as-prepared model materials. The specific capacitance of the Fe/Co/Ni-TMQD@rGO composites is 384.8F g^{-1}, 294.5F g^{-1}, and 354.5F g^{-1} at 10.0 A g^{-1} respectively, which is significantly increased compared to the contrast composite. The difference in specific capacitance of the composites is mainly attributed to the PC contribution and the intercalating effect from TMQDs. Moreover, electrochemical kinetic studies demonstrated that as the scanning speed increases, the SCPs and DCPs gradually approach a dynamic equilibrium state. Additionally, the DCP contributions of the Fe/Co/Ni-TMQD@rGO composites are closely correlated with the number of the valence electrons of ITMEs. The greater the number of valence electrons, the higher the contribution proportion of DCPs to the total capacitance. Further, the contribution proportion of SCPs to the total capacitance is significantly affected by the OH^- adsorption energy of the Fe/Co/Ni-TMQD@rGO composites.

CRediT authorship contribution statement

Yaoning Xi: Conceptualization, Methodology, Software, Data curation, Investigation, Writing – original draft, Visualization. **Jingwang Yan:** Conceptualization, Methodology, Data curation, Writing – review & editing, Supervision, Funding acquisition. **Baigang An:** Conceptualization, Writing – review & editing, Supervision, Project administration, Funding acquisition.

Declaration of Competing Interest

The authors declare that they have no known competing financial interests or personal relationships that could have appeared to influence the work reported in this paper.

Data availability

Data will be made available on request.

Acknowledgements

This work was supported by the National Natural Science Foundation of China (Grant No. 51672118, 51972156, 51872131 and 22179129). Special thanks to Yanmei Li for her assistance in our experiments and Xinliang Wang, Mingchao Zhang for their assistances in the capacitance contribution calculations.

Appendix A. Supplementary data

Supplementary data to this article can be found online at https://doi.org/10.1016/j.apsusc.2023.158121.

References

[1] A. Muzaffar, M.B. Ahamed, K. Deshmukh, J. Thirumalai, A review on recent advances in hybrid supercapacitors: Design, fabrication and applications, Renew. Sustain. Energy Rev. 101 (2019) 123–145, https://doi.org/10.1016/j.rser.2018.10.026.

[2] D.P. Chatterjee, A.K. Nandi, A review on the recent advances in hybrid supercapacitors, J. Mater. Chem. A 9 (2021) 15880–15918, https://doi.org/10.1039/D1TA02505H.

[3] S. Tamang, S. Rai, R. Bhujel, N.K. Bhattacharyya, B.P. Swain, J. Biswas, A concise review on GO, rGO and metal oxide/rGO composites: Fabrication and their supercapacitor and catalytic applications, J. Alloy. Compd. 947 (2023), 169588, https://doi.org/10.1016/j.jallcom.2023.169588.

[4] D.D. Khumujam, T. Kshetri, T.I. Singh, N.H. Kim, J.H. Lee, Hierarchical integrated hybrid structural electrodes based on Co-N/C and Mo-doped NiCo-LDH@Co-N/C Anchored on MX/CF for high energy density fiber-shaped supercapacitor, Adv. Funct. Mater. (2023) 2302388, https://doi.org/10.1002/adfm.202302388.

[5] A. Gupta, C.A. Allison, M.E. Ellis, J. Choi, A. Davis, R. Srivastava, F.M. de Souza, D. Neupane, S.R. Mishra, F. Perez, A. Kumar, R.K. Gupta, T. Dawsey, Cobalt metal–organic framework derived cobalt–nitrogen–carbon material for overall water splitting and supercapacitor, Int. J. Hydrogen Energy 48 (2023) 9551–9564, https://doi.org/10.1016/j.ijhydene.2022.11.340.

[6] F. Yuan, C. Li, J. Wu, Y. Liang, H. Huang, S. Xu, X. Liang, W. Zhou, J. Guo, Binder-free hybrid cobalt-based sulfide/oxide nanoarrays toward enhanced energy storage performance for hybrid supercapacitors, J. Storage Mater. 63 (2023), 106979, https://doi.org/10.1016/j.est.2023.106979.

[7] D. Acharya, I. Pathak, B. Dahal, P.C. Lohani, R.M. Bhattarai, A. Muthurasu, T. Kim, T.H. Ko, K. Chhetri, H.Y. Kim, Immoderate nanoarchitectures of bimetallic MOF derived Ni–Fe–O/NPC on porous carbon nanofibers as freestanding electrode for asymmetric supercapacitors, Carbon 201 (2023) 12–23, https://doi.org/10.1016/j.carbon.2022.08.091.

[8] Y. Wang, Y. Chen, H. Zhao, L. Li, D. Ju, C. Wang, B. An, Biomass-derived porous carbon with a good balance between high specific surface area and mesopore volume for supercapacitors, Nanomaterials 12 (2022) 3804, https://doi.org/10.3390/nano12213804.

[9] C. Zhong, Y. Deng, W. Hu, J. Qiao, L. Zhang, J. Zhang, A review of electrolyte materials and compositions for electrochemical supercapacitors, Chem Soc Rev 44 (2015) 7484–7539, https://doi.org/10.1039/c5cs00303b.

[10] J. Vejpravová, Mixed sp^2–sp^3 nanocarbon materials: A status quo review, Nanomaterials 11 (2021) 2469, https://doi.org/10.3390/nano11102469.

[11] Z. Zhai, L. Zhang, T. Du, B. Ren, Y. Xu, S. Wang, J. Miao, Z. Liu, A review of carbon materials for supercapacitors, Mater. Des. 221 (2022), 111017, https://doi.org/10.1016/j.matdes.2022.111017.

[12] H. Zhao, Y. Zhang, L. Li, X. Geng, H. Yang, W. Zhou, C. Sun, B. An, Synthesis of an ordered porous carbon with the dual nitrogen-doped interfaces and its ORR catalysis performance, Chin. Chem. Lett. 32 (2021) 140–145, https://doi.org/10.1016/j.cclet.2020.11.035.

[13] H. Zhao, L. Li, Y. Liu, X. Geng, H. Yang, C. Sun, B. An, Synthesis and ORR performance of nitrogen-doped ordered microporous carbon by CVD of acetonitrile vapor using silanized zeolite as template, Appl. Surf. Sci. 504 (2020), 144438, https://doi.org/10.1016/j.apsusc.2019.144438.

[14] X. Yang, C. Chi, Y. Wang, Q. Ling, D. Li, Liquid-mediated dense integration of graphene materials for compact capacitive energy storage, Science 341 (2013) 534–537, https://doi.org/10.1126/science.1239089.

[15] Z. Lei, N. Christov, X.S. Zhao, Intercalation of mesoporous carbon spheres between reduced graphene oxide sheets for preparing high-rate supercapacitor electrodes, Energ. Environ. Sci. 4 (2011) 1866–1873, https://doi.org/10.1039/c1ee01094h.

[16] Z. Yu, L. Peng, G. Yu, Electrochemical hierarchical composites, Springer International Publishing, 2015, pp. 239–286, https://doi.org/10.1007/978-3-319-12868-9_7.

[17] T. Rensch, V. Chantrain, M. Sander, S. Grätz, L. Borchardt, Scale-up of solvent-free, mechanochemical precursor synthesis for nanoporous carbon materials via extrusion, ChemSusChem 15 (2022) e202200651.

[18] H. Ma, J. He, D.B. Xiong, J. Wu, Q. Li, V. Dravid, Y. Zhao, Nickel cobalt hydroxide @Reduced graphene oxide hybrid nanolayers for high performance asymmetric supercapacitors with remarkable cycling stability, Acs Appl Mater Interfaces (2016) 1992–2000, https://doi.org/10.1021/acsami.5b10280.

[19] C. Zhang, X. Geng, S. Tang, M. Deng, Y. Du, $NiCo_2O_4$ @rGO hybrid nanostructures on Ni foam as high-performance supercapacitor electrodes, J. Mater. Chem. A 5 (2017) 5912–5919, https://doi.org/10.1039/C7TA00571G.

[20] Q. Wang, L. Jiao, H. Du, Y. Wang, H. Yuan, Fe_3O_4 nanoparticles grown on graphene as advanced electrode materials for supercapacitors, J. Power Sources 245 (2014) 101–106, https://doi.org/10.1016/j.jpowsour.2013.06.035.

[21] S.K. Park, P. Nakhanivej, H.S. Park, Two-dimensional nanomaterials as emerging pseudocapacitive materials, Korean J. Chem. Eng. 36 (2019) 1557–1564, https://doi.org/10.1007/s11814-019-0364-1.

[22] J. Ding, W. Hu, E. Paek, D. Mitlin, Review of hybrid ion capacitors: From aqueous to lithium to sodium, Chem Rev 118 (2018) 6457–6498, https://doi.org/10.1021/acs.chemrev.8b00116.

[23] A. Ehsani, A.A. Heidari, H.M. Shiri, Electrochemical pseudocapacitors based on ternary nanocomposite of conductive polymer/graphene/metal oxide: An introduction and review to it in recent studies, Chem Rec 19 (2019) 908–926, https://doi.org/10.1002/tcr.201800112.

[24] A.A. Herzing, C.J. Kiely, A.F. Carley, P. Landon, G.J. Hutchings, Identification of active gold nanoclusters on iron oxide supports for CO oxidation, Science 321 (2008) 1331–1335, https://doi.org/10.1126/science.1159639.

[25] H.T. Chung, D.A. Cullen, D. Higgins, B.T. Sneed, E.F. Holby, K.L. More, P. Zelenay, Direct atomic-level insight into the active sites of a high-performance PGM-free ORR catalyst, Science 357 (2017) 479–484, https://doi.org/10.1126/science.aan2255.

[26] J. Lin, Y. Chen, Y. Zhou, L. Li, B. Qiao, A. Wang, J. Liu, X. Wang, T. Zhang, More active Ir subnanometer clusters than single-atoms for catalytic oxidation of CO at low temperature, AIChE J 63 (2017) 4003–4012, https://doi.org/10.1002/aic.15756.

[27] J. Jones, H. Xiong, A.T. DeLaRiva, E.J. Peterson, H. Pham, S.R. Challa, G. Qi, S. Oh, M.H. Wiebenga, X.I. Pereira Hernandez, Y. Wang, A.K. Datye, Thermally stable single-atom platinum-on-ceria catalysts via atom trapping, Science 353 (2016) 150–154, https://doi.org/10.1126/science.aaf8800.

[28] M.D. Rossell, F.J. Caparrós, I. Angurell, G. Muller, J. Llorca, M. Seco, O. Rossell, Magnetite-supported palladium single-atoms do not catalyse the hydrogenation of alkenes but small clusters do, Catalysis Science & Technology 6 (2016) 4081–4085, https://doi.org/10.1039/c6cy00596a.

[29] N. Yan, N. Xia, L. Liao, M. Zhu, F. Jin, R. Jin, Z. Wu, Unraveling the long-pursued Au_{144} structure by x-ray crystallography, Sci Adv 4 (2018) eaat7259, https://doi.org/10.1126/sciadv.aat7259.

[30] I. Chakraborty, T. Pradeep, Atomically precise clusters of noble metals: Emerging link between atoms and nanoparticles, Chem Rev 117 (2017) 8208–8271, https://doi.org/10.1021/acs.chemrev.6b00769.
[31] G. Kresse, D. Joubert, From ultrasoft pseudopotentials to the projector augmented-wave method, Phys. Rev. B 59 (1999) 1758–1775, https://doi.org/10.1103/PhysRevB.59.1758.
[32] B. Hammer, L.B. Hansen, J.K. Nørskov, Improved adsorption energetics within density-functional theory using revised Perdew-Burke-Ernzerhof functionals, Phys. Rev. B 59 (1999) 7413–7421, https://doi.org/10.1103/PhysRevB.59.7413.
[33] J.P. Perdew, K. Burke, M. Ernzerhof, Generalized gradient approximation made simple, Phys Rev Lett 77 (1996) 3865–3868, https://doi.org/10.1103/PhysRevLett.77.3865.
[34] P.E. Blochl, Projector augmented-wave method, Phys Rev B Condens Matter 50 (1994) 17953–17979, https://doi.org/10.1103/physrevb.50.17953.
[35] P. Pachfule, D. Shinde, M. Majumder, Q. Xu, Fabrication of carbon nanorods and graphene nanoribbons from a metal–organic framework, Nat. Chem. (2016) 718–724, https://doi.org/10.1038/nchem.2515.
[36] X. Pu, D. Zhao, C. Fu, Z. Chen, S. Cao, C. Wang, Y. Cao, Understanding and calibration of charge storage mechanism in cyclic voltammetry curves, Angew. Chem. Int. Ed. 60 (2021) 21310–21318, https://doi.org/10.1002/anie.202104167.